Nucleon knockout on Argon

A. M. Kelly[1, 2]

[1] *Theoretical Physics Department, Fermilab, Batavia IL 60510, USA*
[2] *Department of Physics and Astronomy, University of Kentucky, Lexington KY 40506, USA*

We analyze nucleon knockout observables for semi-inclusive scattering off Argon. We compare different theoretical approaches, including the effects of distorted waves, spectral functions, optical potentials, and nucleon rescattering. We provide analysis of the recent data from MicroBooNE and study observables measurable in LArTPCs. We find, by comparing calculations with realistic spectral functions for different nuclei, that observables, in the MicroBooNE experiment, are indistinguishable with the current experimental precision. We apply an Intra-Nuclear Cascade (INC) model from the NEUT event generator to RDWIA and RPWIA calculations for ^{40}Ar. The Relativistic Optical Potential (ROP) under-predicts the MicroBooNE data significantly suggesting inelastic FSI events contribute and this is shown with a comparison with INC that only include elastic channels. Additionally, we find that distorted wave calculations feature a significant reduction in the observables compared to plane wave calculations. These differences remain even after applying an INC model. After cascades both under-predict the data but yield the correct shape in most cases. Non-Quasielastic effects, which are not accounted for in this study, may contribute to the high missing momentum region. Other notable discrepancies include an under-prediction in the low missing momentum region which will require further study.

I. INTRODUCTION

Neutrinos are a promising area of study for beyond standard model physics but, in order to gain a better understanding of neutrinos, we must study neutrino-nucleus scattering. In neutrino-nucleus scattering, an oncoming neutrino scatters and interacts weakly with one of the nucleons in the nucleus. In some cases, you can have so-called Neutral-Current (NC) interactions where a neutrino exchanges a Z^0 particle with a neutron resulting in no electric charge in the final state. Most current interest is in Charged-Current (CC) interactions where a neutrino exchanges a W^+ particle with a neutron, in which, the neutrino becomes a charged lepton and the neutron can become a proton in a process similar to beta decay. In principle, the neutrino could exchange a W^- as well with a proton which results in a charged lepton and a neutron in the final state.

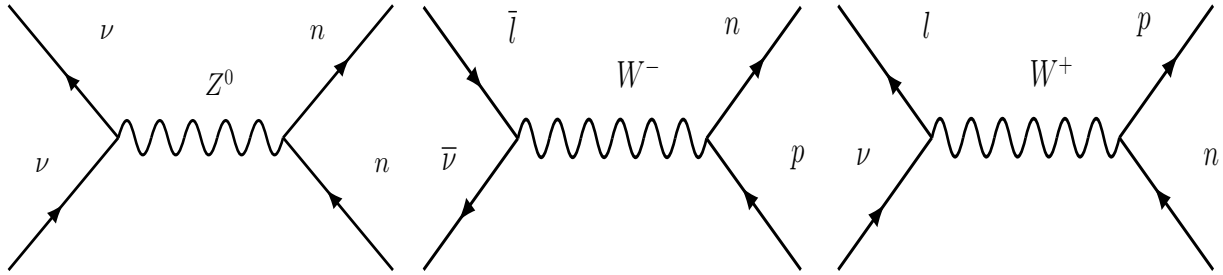

FIG. 1. Diagram representations of neutral (left) and charged-current (center and right) neutrino-nucleus interactions.

If enough energy and momentum are transferred to the nucleon, it can get knocked out of the nucleus. We call this a CC1p0π event

$$\nu + A \longrightarrow \mu + P + X \tag{1}$$

where ν, A, μ, and P refer to the neutrino, the nucleus, the muon, and the proton respectively. X denotes the residual hadronic system that remains unobserved. Since neutrino beams are not monochromatic in energy, an energy reconstruction is necessary to learn about individual neutrino-nucleus scattering events. Theoretical models and simulations are used to calculate the cross-sections of these events which is proven to be a difficult task for nuclear theory. Final-State Interactions (FSI) between the outgoing proton and the dense nuclear medium are not entirely well understood but are necessary to describe the missing kinematics. Event generators typically use Intra-Nuclear Cascade (INC) models to simulate the effects of FSI.

In a CC1p0π event, we can define the semi-inclusive flux-averaged cross-section as

$$\left\langle \frac{d^6\sigma}{d|\vec{k}_f|d\cos\theta_f d|\vec{k}_N|d\Omega_N} \right\rangle = \int dE_m \tilde{\Phi}(E_i) \frac{d^6\sigma}{d|\vec{k}_f|d\cos\theta_f d|\vec{k}_N|d\Omega_N} \tag{2}$$

where $\tilde{\Phi}(E_i)$ is the normalized neutrino flux, E_i and E_m are the incident neutrino energy and missing energy, respectively. It is more common to define the cross-section in terms of the missing energy [1] given by:

$$\left\langle \frac{d^6\sigma}{d|\vec{k}_f|d\cos\theta_f d|\vec{k}_N|d\Omega_N} \right\rangle = \int dE_m \phi(E)\rho(E_m)\mathcal{F} \frac{k_l^2 p_N^2 M_B^*}{(2\pi)^5 E_B f_{rec}} l_{\mu\nu} H^{\mu\nu} \tag{3}$$

where $\rho(E_m)$ is a realistic energy density, $l_{\mu\nu}$ is the lepton tensor, and $H^{\mu\nu}$ is the hadron tensor which includes high-momentum components from short-range correlations. In the following sections, we compute the fully differential unfactorized semi-inclusive cross-section in the Relativistic Distorted Wave Impulse Approximation (RDWIA) and compare it to MicroBooNE data. The MicroBooNE experiment is the first of its kind to feature double-differential cross-section measurements which could allow for one to find a region in the phase space in which the RDWIA fits the data well.

II. MICROBOONE DATA

The MicroBooNE collaboration has recently published measurements of the semi-inclusive charged current $^{40}\mathrm{Ar}(\nu_\mu, \mu p)X$ reaction [2]. We applied the same bins that MicroBooNE uses as well as their kinematic cuts.

These include cuts on the proton momentum where only events with a single proton in the range $300 < p^p < 1000$ MeV and a muon in the range $100 < p^\mu < 1200$ MeV pass. Additionally, there is a cutoff on charged pions such that events with pions with momenta $p_\pi > 70$ MeV are excluded. Neutral pions of any momentum were excluded. Data is reported in terms of variables that measure the transverse kinematics imbalance.

We can assign four-momentum vectors to the neutrino (P^μ_ν), the muon (P^μ_μ), the nucleus (P^μ_A), and the proton (P^μ_N). Using energy-momentum conservation, yields

$$P^\mu_\nu + P^\mu_A = P^\mu_\mu + P^\mu_N + P^\mu_X \tag{4}$$

where P^μ_X is the four-momentum of the residual hadron system that remains unobserved. The missing momentum, $\vec{p}_m$, is defined as $\vec{p}_m \equiv \vec{p}_\mu + \vec{p}_N - \vec{p}_\nu$. If we only look at the momentum transverse to the beam direction, then $p^\nu_T = 0$ because the neutrino is fixed along the z-direction and $p^A_T = 0$ because the nucleus is in the rest frame. The component of the missing momentum transverse to the beam is

$$\delta\vec{p_T} \equiv \vec{p}_{\mu,T} + \vec{p}_{N,T} \tag{5}$$

where $\vec{p}_{\mu,T}$ and $\vec{p}_{N,T}$ are the transverse momenta of the proton and muon, respectively. The angle with respect to $\vec{p}_{\mu,T}$ expressed as

$$\delta\alpha_T \equiv arccos\left(\frac{-\vec{p}_{\mu,T}\cdot\delta\vec{p}_T}{p_{\mu,T}\delta p_T}\right) \tag{6}$$

and with that, we can define the x and y components of δp_T as

$$\begin{aligned}\delta p_{T,x} &\equiv (\hat{p}_\nu \times \hat{p}_{\mu,T})\cdot\delta\vec{p}_T \\ \delta p_{T,y} &\equiv -\hat{p}_{\mu,T}\cdot\delta\vec{p}_T\end{aligned} \tag{7}$$

where we can see the lepton plane is the y-z plane and the x-axis is perpendicular to that plane. The opening angle between the outgoing muon and proton pair in the transverse plane is defined as

$$\delta\phi_T \equiv arccos\left(\frac{-\vec{p}_{\mu,T}\cdot\vec{p}_{N,T}}{p_{\mu,T}p_{N,T}}\right) \tag{8}$$

where $\delta\phi_T$ is the opening angle. It is common in neutrino experiments to define a calorimetric energy reconstruction, E_{cal}, of the incoming neutrino, which in microBooNE, E_{cal} is defined as

$$E_{cal} \equiv E_\mu + T_p + BE \tag{9}$$

where E_μ is the muon energy, T_p is the proton's kinetic energy, and BE is the average binding energy of Ar40 which taken to be 0.04 GeV in Ref. [2]. We compute an average neutrino energy, as a function of the measured kinematics, defined as

$$\langle E_{avg}\rangle \equiv \frac{\int dE E\phi(E)\frac{d^6\sigma(E)}{d\Omega_l dk_l d\Omega_N dp_N}}{\int dE\phi(E)\frac{d^6\sigma(E)}{d\Omega_l dk_l d\Omega_N dp_N}} \tag{10}$$

where $\phi(E)$ is a flux distribution and $\frac{d^6\sigma(E)}{d\Omega_l dk_l d\Omega_N dp_N}$ is the six-fold differential cross-section with the measured kinematic variables fixed.

III. RESULTS

We plot the differential cross section as functions of the previous kinematic variables to see the effects of final state interactions (FSI) and to study A-dependence in the observables. We use models suitable for describing the kinematics of exclusive 1-nucleon knockout. All these approaches use a realistic spectral function. In the Relativistic Plane Wave Impulse Approximation (RPWIA), FSI is completely neglected and the outgoing nucleon is a plane wave.

The Spectral Function Approach (SFA), or more accurately the plane-wave impulse approximation (PWIA) uses a factorized form of the cross section [3, 4]. Elastic FSI, can be included by treating the outgoing nucleon as a scattering state in a potential, this is crucial in order to describe the inclusive cross section [5]. We use for this the Energy-Dependent Relativistic Mean-Field (EDRMF) model. The EDRMF includes a phenomenological factor that weakens the potential for greater nucleon energy, but is equal to the RMF potential at low energy [5, 6]. Additionally, we use a Relativistic Optical Potential (ROP) of Ref. [7] where the imaginary component acts as an absorbing term, this absorptive part removes strength lost to inelastic channels. Events distributed according to the flux-averaged fivefold differential cross section are generated using an event generator code in C++. The resulting events are then fed into a Python script where the previous kinematic variables are computed explicitly. The differential cross-section is then determined as

$$\frac{\sigma_{tot}}{N_{tot}} \frac{N_B}{\prod_{i=1}^{n} B_{X_i}} \tag{11}$$

where σ_{tot} denotes the total cross-section, N_{tot} is the total number of events, N_B is the number of events in the bin, δX is the observable of interest (e.g. δp_T), and B_X is the binwidth used for the observable.In the following sections, we only use a subset of the data from MicroBooNE [2] and we use MicroBooNE's binwidths for comparison. The full data set is given in Appendix A.

A. A-Dependence of Observables

Neutrino experiments use a variety of nuclear targets, e.g. MiniBooNE used ^{12}C, T2(H)K uses ^{16}O, and SBND, MicroBooNE and DUNE use ^{40}Ar. It is thus paramount to understand and describe interactions off different targets. For inclusive interactions, e.g. (e, e') experiments it is established that A-scaling works fairly well in the quasi-elastic region at sufficient momentum transfer. This means that inclusive interactions off different targets can be described with a single scaling function, that is independent of the target, in addition to and a momentum scale (the fermi momentum), and an energy scale (the separation energy) that depend weakly on the target nucleus [8].

We study flux-integrated semi-inclusive cross-sections for ^{40}Ar, ^{40}Ca, ^{12}C, and ^{16}O. We use the PWIA along with realistic spectral functions for the different targets [1, 9]. The different missing-momentum profiles encoded in the spectral functions will affect the observables, mostly notably, δp_T. Additionally, the unique shell structure (i.e. missing energy profiles) of the targets may affect results to a lesser extent. We plot the differential cross-section as a function of δp_T for different nuclei obtained with the SFA in Fig. 2 below.

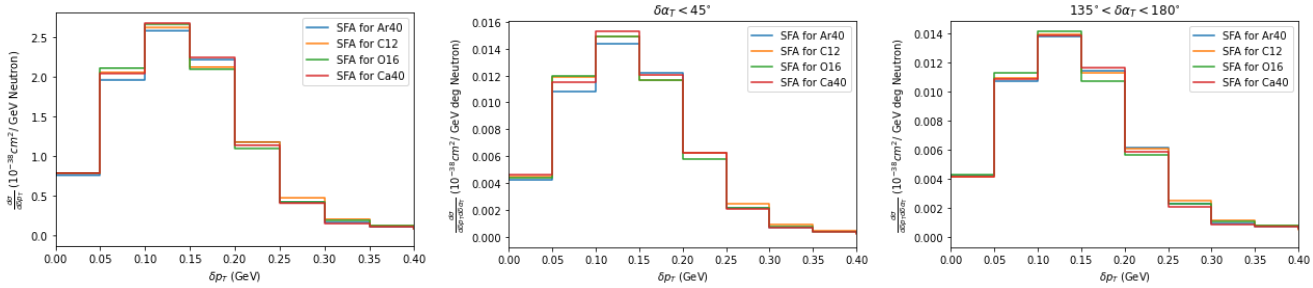

FIG. 2. The flux-averaged single- (left) double-differential cross sections as functions of δp_T and $\delta\alpha_T$, for ^{40}Ar, ^{40}Ca, ^{12}C, and ^{16}O.

We can see little difference between different nuclei with the SFA indicating that the observables are not sensitive to the differences in the spectral functions after flux-averaging. The total cross-sections used for each target are in Table. I below. If we plot the theoretical momentum density from the SFA, we can see differences as shown in Fig. 3. We can see that ^{40}Ar and ^{40}Ca behave similarly but both are noticeably different from ^{12}C and ^{16}O. We expect these differences between nuclei due to different shell structures which are incorporated into the spectral function and lead to different momentum distributions. These differences do not emerge in Fig. 2 because of the flux-averaging that is done in MicroBooNE and the relatively large bin sizes.

It is worth noting, that these comparisons were done prior to the incorporation of FSI. In the following sections, we study RPWIA and RDWIA calculations prior to FSI and after FSI with ^{40}Ar as the target.

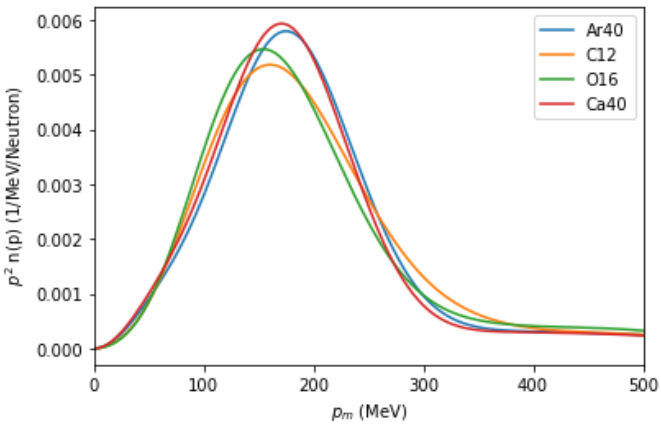

FIG. 3. The missing momentum density per neutron, where p^2 is a geometric factor, of the different targets as functions of missing momentum p_m.

Targets	σ_{tot} (10^{-42} cm^2)	σ_{tot} (10^{-42} cm^2)/neutron
C12	40824.26	6804.04
O16	54529.10	6816.13
Ca40	136884.74	6844.23
Ar40	151110.36	6868.65

TABLE I. The total cross-sections and total cross-sections per neutron for every element.

B. Elastic FSI in the RDWIA

We compare the previously mentioned models to MicroBooNE data before including inelastic FSI. We can see in Fig. 4 that our models, except the ROP, over-predict the cross-section in the $0.1 < \delta p_T < 0.3$ GeV range as well as under-predicting at higher momentum in the single-differential cross-section. These discrepancies are due to FSI where the nucleon rescatters. In general, nucleon re-scattering leads to a greater missing momentum which would explain the over-prediction at low missing momenta and the corresponding under-predictions at higher momenta. Additionally, we can see that the SFA and RPWIA models give nearly equivalent descriptions and a similar case can be made for the rROP and EDRMF models. For this reason, the following plots will only use RPWIA and EDRMF.

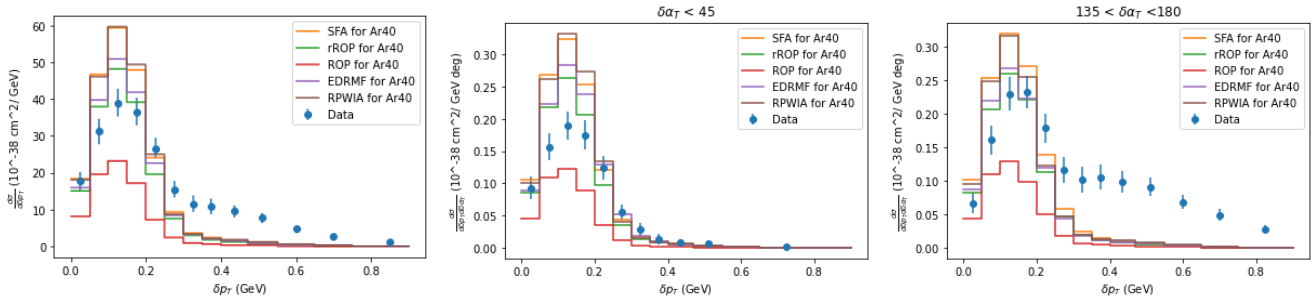

FIG. 4. The flux-averaged single- (left) and double- differential cross sections as functions of δp_T and $\delta\alpha_T$, compared to MicroBooNE data [2] These models do not consider FSI effects.

In the double differential cross-sections, in Fig. 4, we see for small values of $\delta\alpha_T$ similar over-predictions at low momenta. When $\delta\alpha_T$ and δp_T are large, we can see enhancement of the cross-section suggesting events migrate to this region as expected. The ROP model under-predicts the cross-section because the ROP contains an imaginary component that acts as an absorption term. The ROP model absorbs inelastic FSI events and so the ROP predicts the cross-section where inelastic scattering removes contributions to the cross-section.

C. FSI Cascade Results

To account for inelastic FSI, we make use of the intranuclear cascade model (INC) of the NEUT event generator [10] and apply it to the RPWIA and EDRMF as in Ref. [11]. In Fig. 5 below, we can see the change in the distribution of the most energetic proton per event due to FSI. We see a shift towards lower p_N because the leading proton loses momentum in FSI. This momentum is redistributed over other final-state particles, hence increasing the missing momentum. We also note a build-up of events at low momentum that correspond to inelastic FSI effects. In the event selection, if we only consider elastic events (1-track), i.e. events that do not undergo rescattering in the INC, we see the EDRMF and RPWIA approach the ROP, as was shown previously [11]. The middle panel of Fig. 5 corresponds to the momentum distribution with MicroBooNE cuts applied Where can clearly see the effects of inelastic FSI.

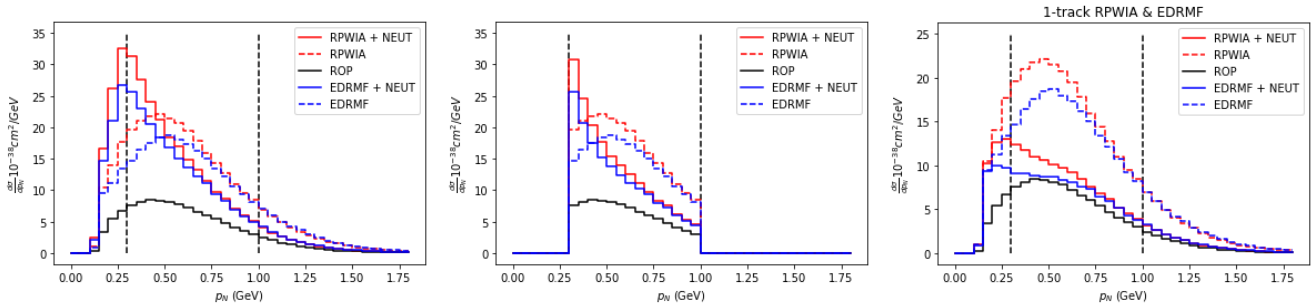

FIG. 5. The flux-averaged single-differential cross sections as a function of p_N with MicroBooNE cutoffs shown as vertical dashed lines. 1-track (right) means only elastic FSI events were considered.

We can see that the RPWIA and EDRMF more accurately represent the data when NEUT is applied as shown in Fig. 6. Strength is removed from the low δp_T region and is moved to higher δp_T and $\delta\alpha_T$. The models do not reproduce the data. This could be due to non-Quasi-Elastic (QE) interactions such as Meson-Exchange Current (MEC) or Resonance (RES). In the lowest δp_T bin, the cascade appears to remove contributions that still appear in the data. What is interesting is that in the large $\delta\alpha_T$ and low δp_T bin, we see better agreement with data.

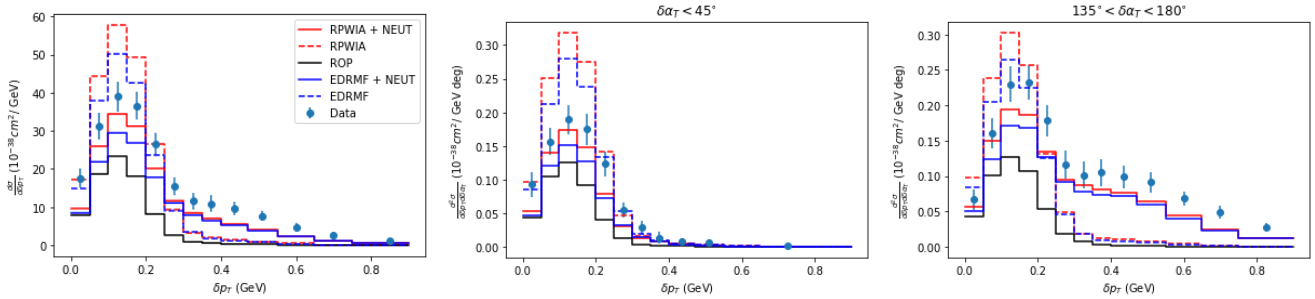

FIG. 6. The flux-averaged single- (left) and double- differential cross sections as functions of δp_T and $\delta\alpha_T$, compared to MicroBooNE data.

The differential cross-section as a function of $\delta\alpha_T$, as well as δp_T for the double differential, is shown in Fig. 7. We expect to see, without FSI, that $\delta\alpha_T$ is flat due to Fermi motion being isotropic [2]. However, when FSI is accounted for, we see strength migrate from the low $\delta\alpha_T$ region to the high $\delta\alpha_T$ region as well as an overall reduction in strength. Interestingly, the NEUT cascade does not appear to predict the increase followed by a sudden decrease that can be seen in the double-differential cross-sections where $\delta p_T < 0.2$ and $0.2 < \delta p_T < 0.4$. This trend is also observed when $\delta\alpha_T$ is binned with $\cos\theta_p$ in Fig. 14 This suggests there could be a contribution from a mechanism outside of the cascade model.

The cross-section in terms of x and y components of δp_T, defined in Eq. 7 as shown in Fig. 8. We can see that prior to FSI, we under-predict at large values of $\delta p_{T,y}$ and we over-predict at low $\delta p_{T,y}$ and $\delta p_{T,x}$ as we would expect. What is interesting, is the difference in the shape of the leftmost and rightmost distribution. Our models replicate these shapes after applying a cascade suggesting FSI preferentially moves strength to large negative $\delta p_{T,y}$ and large $|\delta p_{T,x}|$. Under-predictions at large $\delta p_{T,y}$ and $\delta p_{T,x}$ are expected due to non-QE interactions. However, we can see there is an under-prediction in the low $\delta p_{T,x}$ and $\delta p_{T,y}$ range after FSI similar to the under-prediction in the lowest

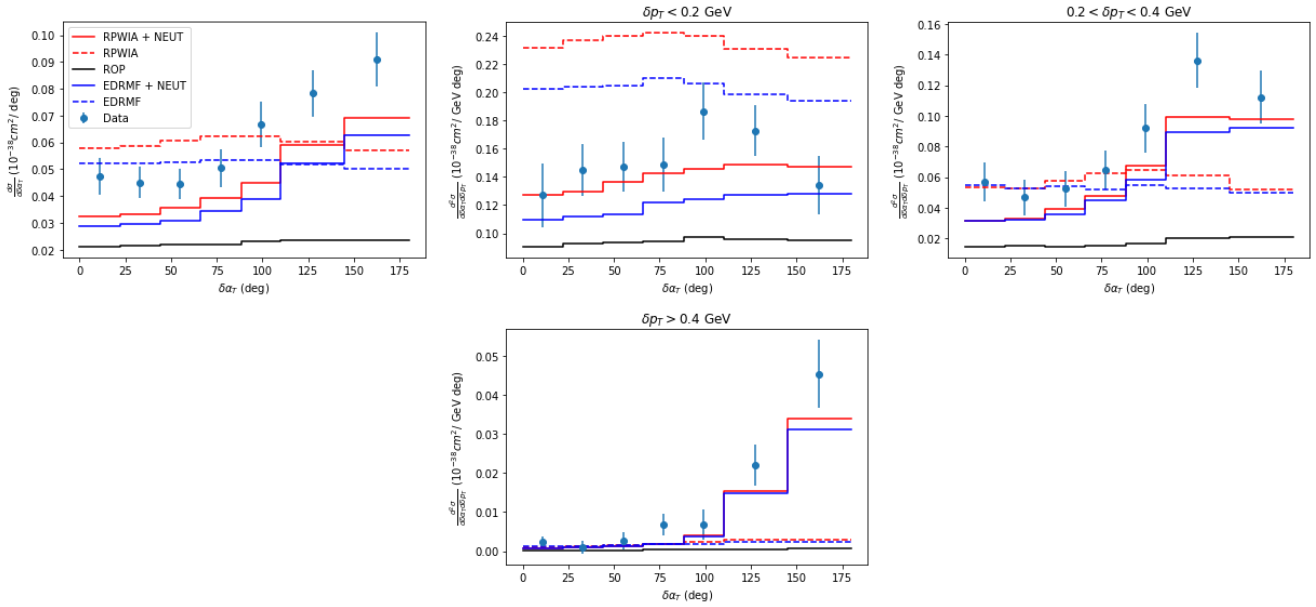

FIG. 7. The flux-averaged single- (top-left) and double-differential cross sections as functions of $\delta\alpha_T$ and δp_T, compared to MicroBooNE data.

bin from the δp_T distribution.

In general, we see the expected trend from applying NEUT to the RPWIA and EDRMF. However, we do see some discrepancies in the low δp_T bin and the $\delta\alpha_T$ distribution in the double-differential. These contributions are likely not due to non-QE processes since we expect that at low δp_T, QE processes dominate. Furthermore, it is unclear if non-QE effects such as MEC or RES could explain the bumps in the $\delta\alpha_T$ double-differential distributions.

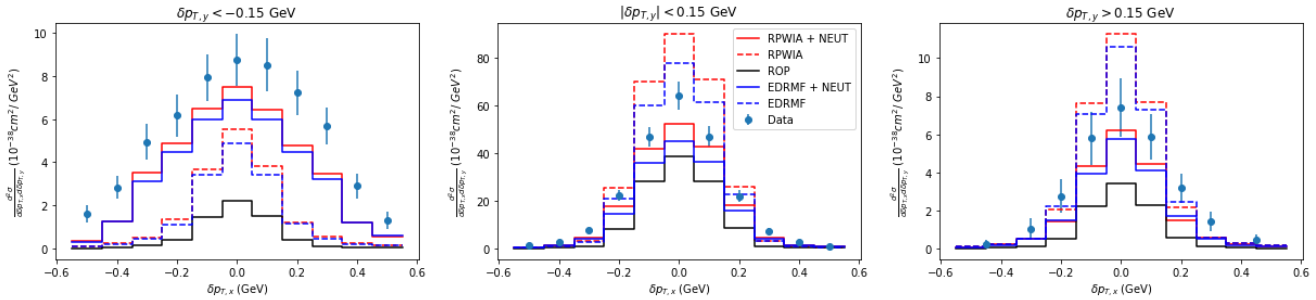

FIG. 8. The flux-averaged double-differential cross sections as functions of $\delta p_{T,x}$ and $\delta p_{T,y}$, compared to MicroBooNE data.

IV. CONCLUSION

We have analyzed and compared the sensitivity of observables from semi-inclusive interactions for different nuclear targets, distorted waves, and FSI. We compare theoretical models to data collected by the MicroBooNE experiment [2]. We found that through MicroBooNE's current binning, observables are roughly indistinguishable after flux-averaging despite differences in the spectral functions of the different targets. This suggests uncertainties on and reasonable changes to the spectral function will result in negligible changes in the observables.

We also compared different theoretical models in which we observed the EDRMF/rROP models predict a weaker signal when compared to RPWIA/SFA models in the low δp_T region. These differences persisted even after the inclusion of NEUT. The ROP under-predicts the cross-section across the board and when compared to cascades provided by NEUT, we see inelastic FSI indeed provides a large contribution hence the under-prediction by the ROP. Furthermore, we have shown that the '1-track' INC events are very similar to the ROP through the p_N distribution.

Future studies will include other observables and different INC models. The INC model from NEUT has been shown to bring protons down from above the 1GeV threshold which then contributes to the signal.

When the cascade from NEUT is applied to the RPWIA and EDRMF models, we under-predict the data which, in part, can be attributed to not including non-QE interactions such as MEC which has been shown to provide large contributions from low to high δp_T in Ref. [2]. It is unclear, however, how such interactions could contribute to the lowest δp_T bin. Interference from 1 and 2 body currents [12] or an increase in the unconstrained axial form factor could possibly enhance this region. It could also be the case that the NEUT INC model over-predicts the amount of re-scattering which motivates a future study where we can compare different INC models. We also see an incorrect description of the shape of the high $\delta\alpha_t$ bins in the double-differential cross-sections with small δp_T. Due to the large uncertainties in the data, it is not clear whether this is an actual discrepancy, however, this shape is reproduced in Ref. 14.

V. ACKNOWLEDGEMENTS

This manuscript has been authored by Fermi Research Alliance, LLC under Contract No. DE-AC02-07CH11359 with the U.S. Department of Energy, Office of Science, Office of High Energy Physics. This work was supported in part by the U.S. Department of Energy, Office of Science, Office of Workforce Development for Teachers and Scientists (WDTS) under the Science Undergraduate Laboratory Internships Program (SULI). I would like to thank my advisor, Alexis Nikolakopoulos, for his guidance on this project. I would also like to thank Vishvas Pandey for the valuable discussions on this work.

[1] R. González-Jiménez, M. B. Barbaro, J. A. Caballero, T. W. Donnelly, N. Jachowicz, G. D. Megias, K. Niewczas, A. Nikolakopoulos, J. W. Van Orden, and J. M. Udías, Phys. Rev. C **105**, 025502 (2022).
[2] P. Abratenko *et al.* (MicroBooNE), (2023), arXiv:2301.03706 [hep-ex].
[3] O. Benhar, V. R. Pandharipande, and S. C. Pieper, Rev. Mod. Phys. **65**, 817 (1993).
[4] N. Rocco, S. X. Nakamura, T. S. H. Lee, and A. Lovato, Phys. Rev. C **100**, 045503 (2019), arXiv:1907.01093 [nucl-th].
[5] R. González-Jiménez, A. Nikolakopoulos, N. Jachowicz, and J. M. Udías, Phys. Rev. C **100**, 045501 (2019).
[6] R. González-Jiménez, M. Barbaro, J. Caballero, T. Donnelly, N. Jachowicz, G. Megias, K. Niewczas, A. Nikolakopoulos, and J. Udías, Phys. Rev. C **101**, 015503 (2020), arXiv:1909.07497 [nucl-th].
[7] E. D. Cooper, S. Hama, and B. C. Clark, Phys. Rev. C **80**, 034605 (2009).
[8] R. González-Jiménez, G. D. Megias, M. B. Barbaro, J. A. Caballero, and T. W. Donnelly, Phys. Rev. C **90**, 035501 (2014).
[9] O. Benhar, A. Fabrocini, S. Fantoni, and I. Sick, Nuclear Physics A **579**, 493 (1994).
[10] Y. Hayato and L. Pickering, Eur. Phys. J. ST **230**, 4469 (2021), arXiv:2106.15809 [hep-ph].
[11] A. Nikolakopoulos, R. González-Jiménez, N. Jachowicz, K. Niewczas, F. Sánchez, and J. M. Udías, Phys. Rev. C **105**, 054603 (2022), arXiv:2202.01689 [nucl-th].
[12] T. Franco-Munoz, J. García-Marcos, R. González-Jiménez, and J. M. Udías, (2023), arXiv:2306.10823 [nucl-th].

Appendix A: Data

We show comparisons to MicroBooNE data in Figs. (10-19). In Fig. 9 below, we compare two different methods for computing the neutrino energy and see that they are in agreement.

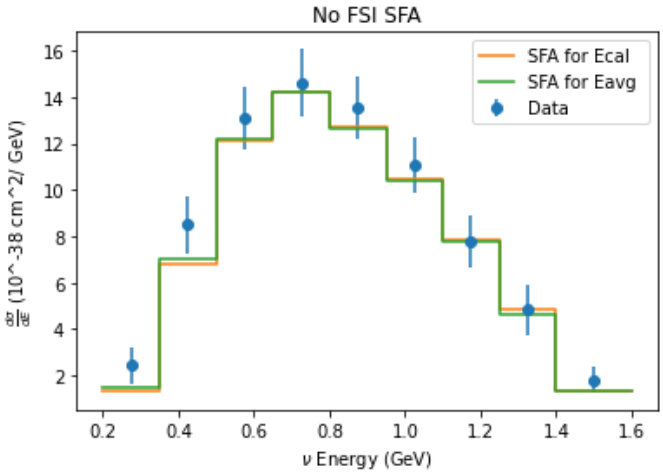

FIG. 9. The flux-integrated single-differential cross-section as a function of the neutrino energy, E_{cal} and E_{Avg}, compared to MicroBooNE data.

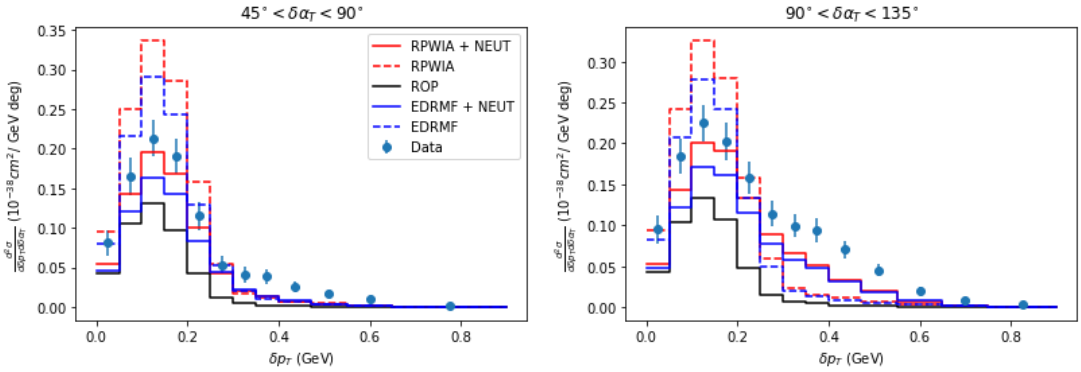

FIG. 10. The flux-averaged double differential cross section as a function of δp_T and $\delta\alpha_T$, compared to MicroBooNE data.

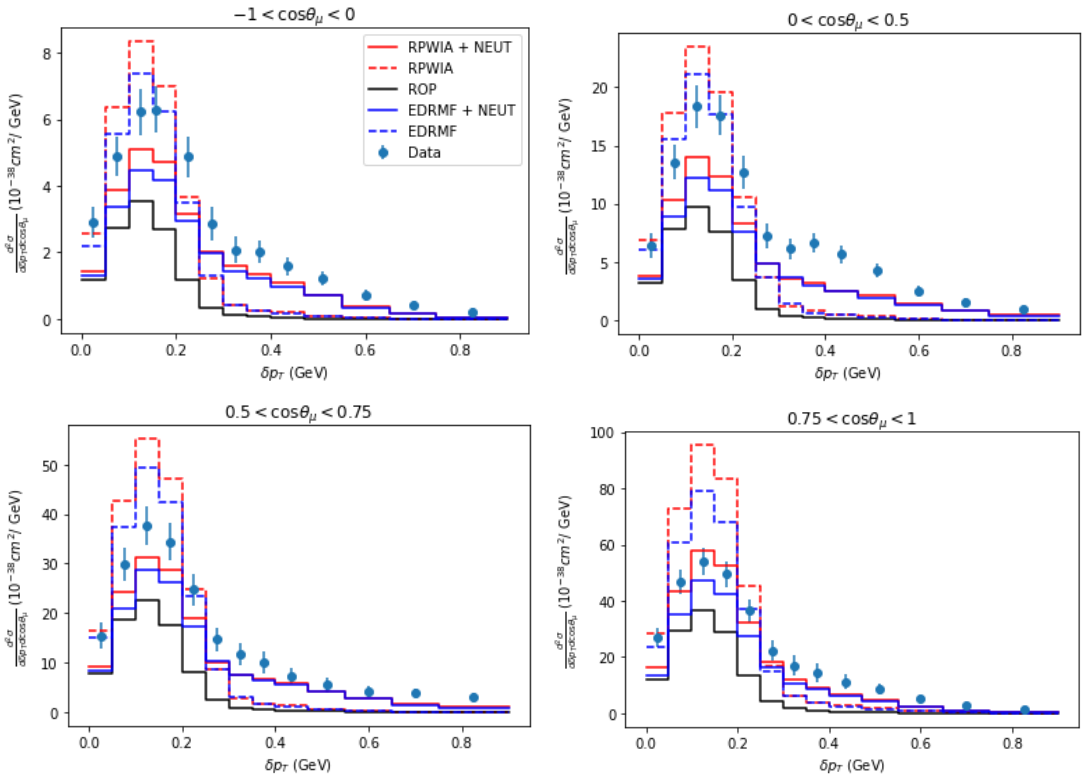

FIG. 11. The flux-averaged double differential cross section as a function of δp_T and $\cos\theta_\mu$, compared to MicroBooNE data.

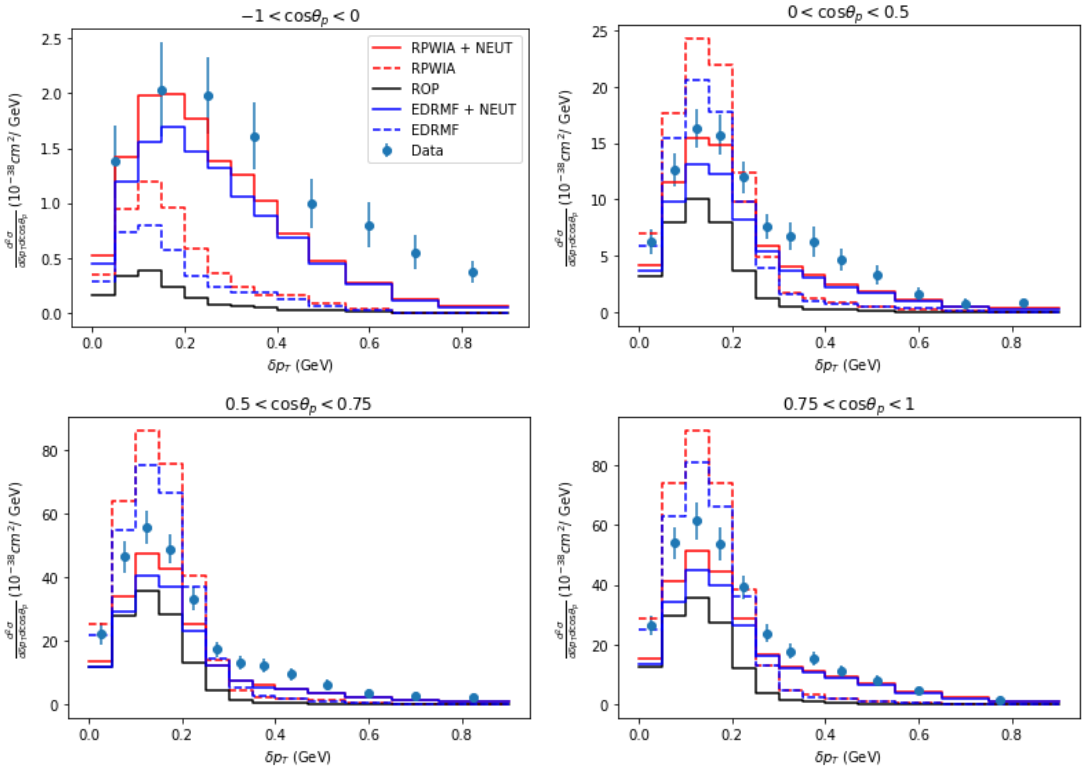

FIG. 12. The flux-averaged double differential cross section as a function of δp_T and $\cos\theta_p$, compared to MicroBooNE data.

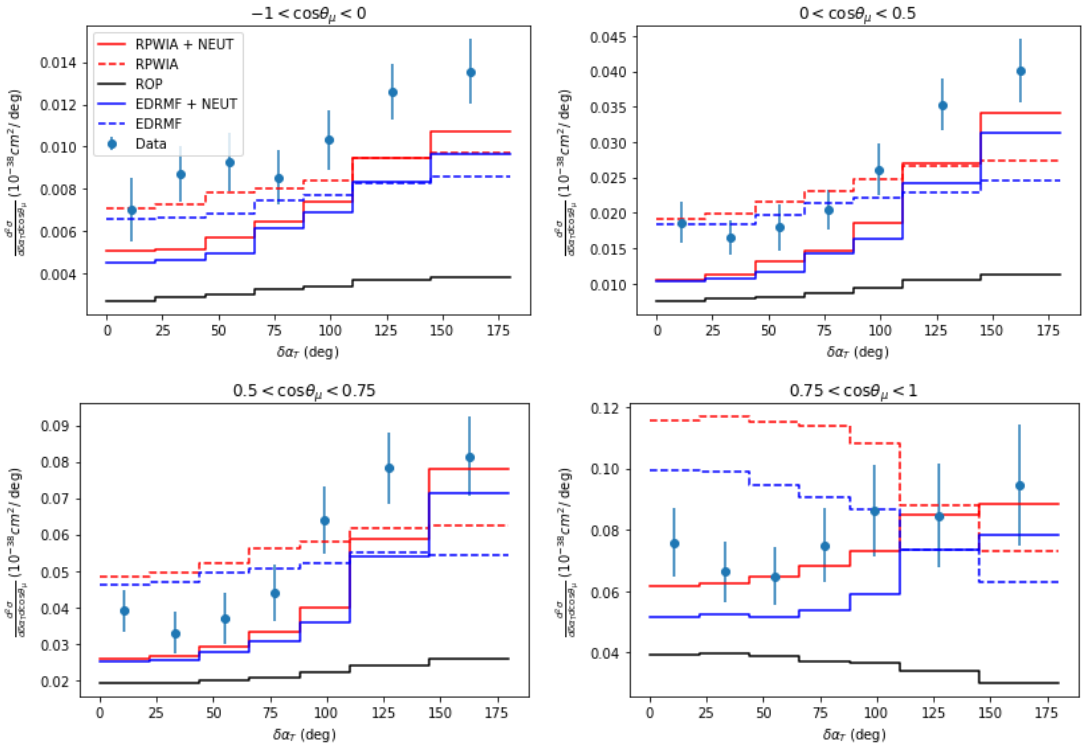

FIG. 13. The flux-averaged double differential cross section as a function of $\delta\alpha_T$ and $\cos\theta_\mu$, compared to MicroBooNE data.

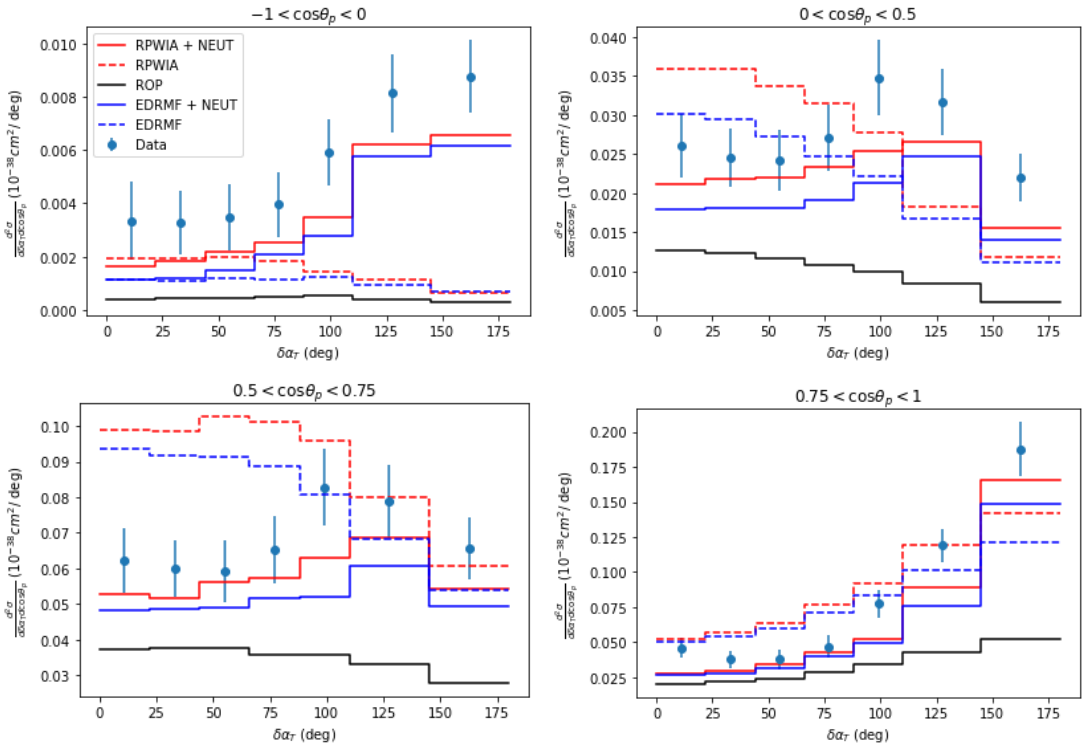

FIG. 14. The flux-averaged double differential cross section as a function of $\delta\alpha_T$ and $\cos\theta_p$, compared to MicroBooNE data.

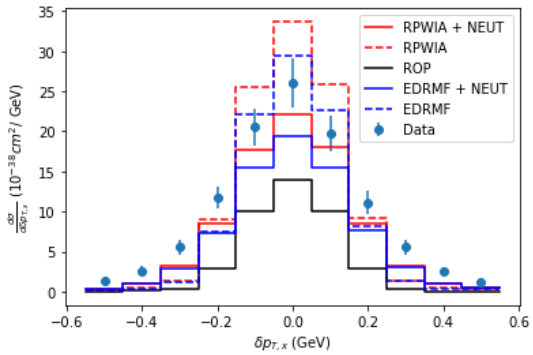

FIG. 15. The flux-averaged single differential cross section as a function of $\delta p_{T,x}$, compared to MicroBooNE data.

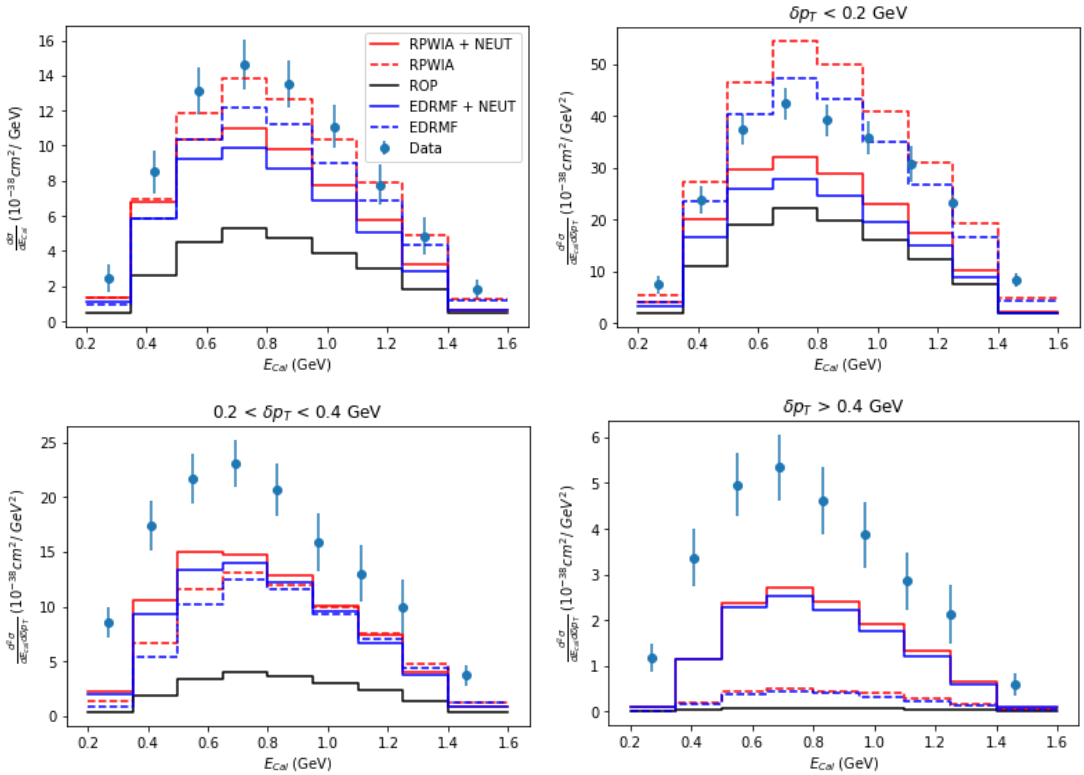

FIG. 16. The flux-averaged single-(top left) and double-differential cross section as a function of E_{Cal} and δp_T, compared to MicroBooNE data.

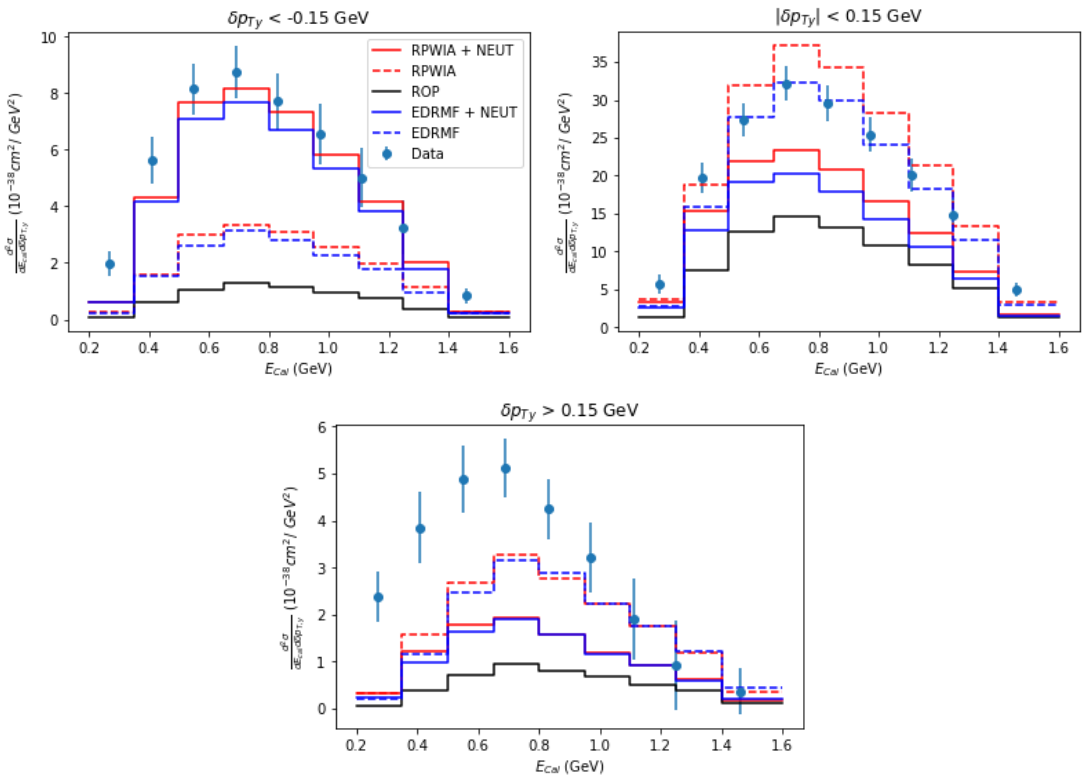

FIG. 17. The flux-averaged double-differential cross section as a function of E_{Cal} and $\delta p_{T,x}$, compared to MicroBooNE data.

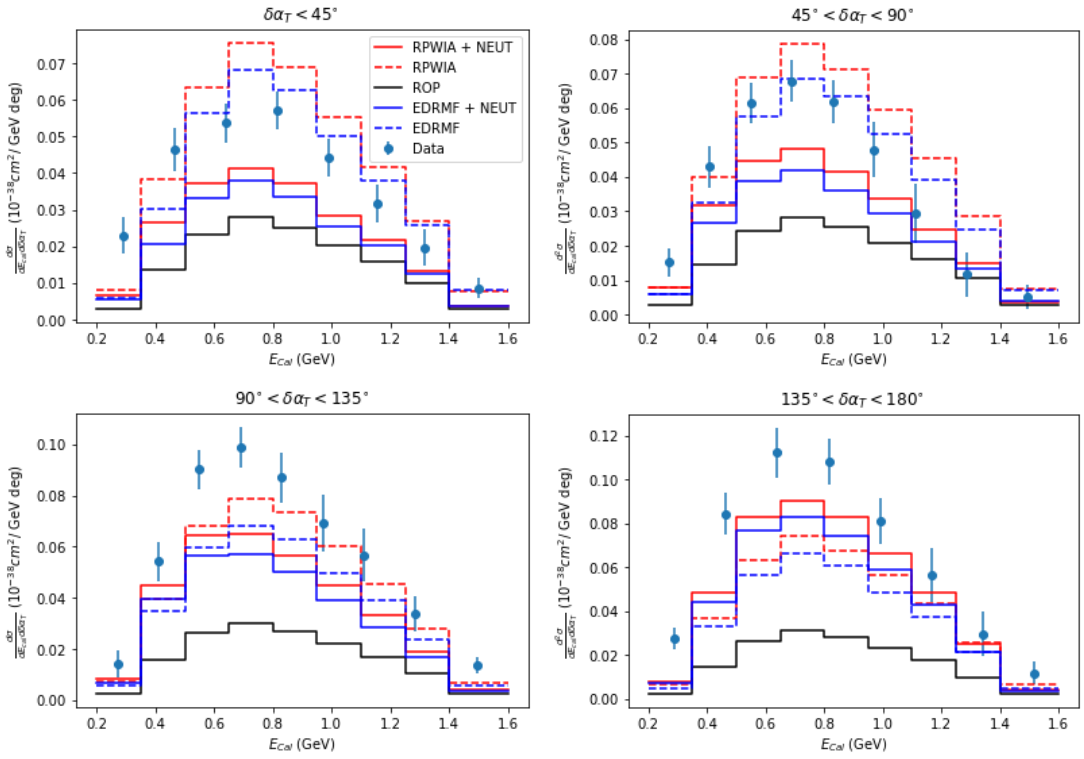

FIG. 18. The flux-averaged double-differential cross section as a function of E_{Cal} and $\delta\alpha_T$, compared to MicroBooNE data.

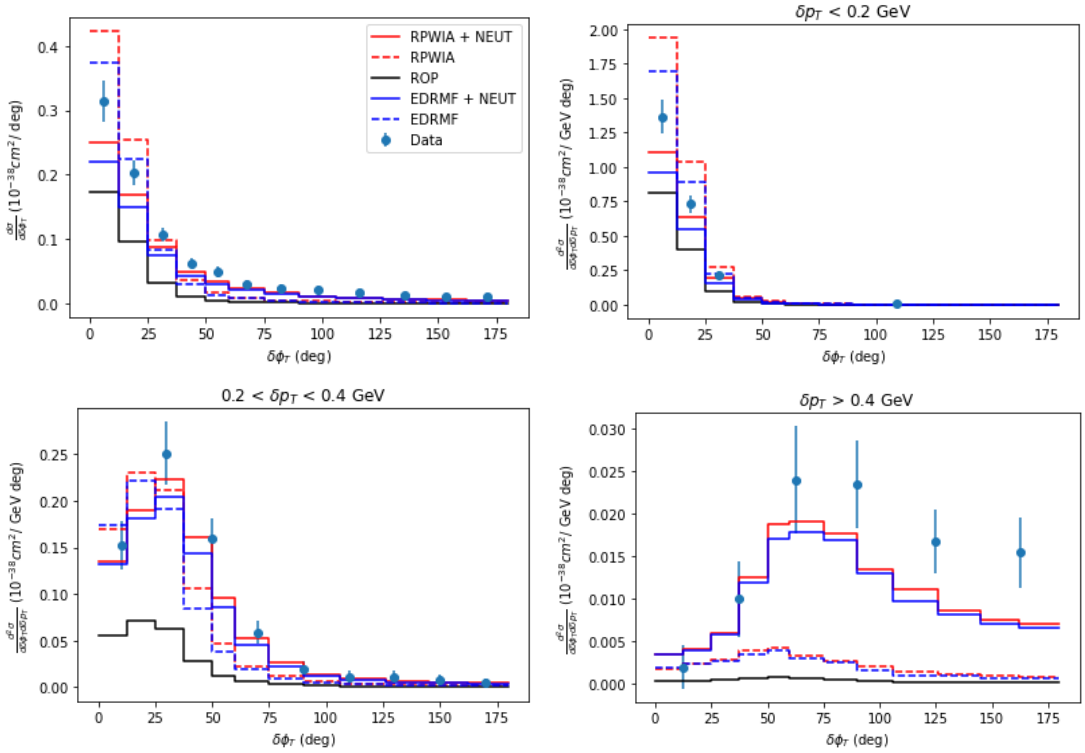

FIG. 19. The flux-averaged double-differential cross section as a function of $\delta\phi_T$ and δp_T, compared to MicroBooNE data.